ARTICLES
https://doi.org/10.1038/s41567-022-01725-6

nature physics

Observation of antiferromagnetic correlations in an ultracold SU(N) Hubbard model

Shintaro Taie[1✉], Eduardo Ibarra-García-Padilla[2], Naoki Nishizawa[1], Yosuke Takasu[1], Yoshihito Kuno[3], Hao-Tian Wei[2,4], Richard T. Scalettar[5], Kaden R. A. Hazzard[2] and Yoshiro Takahashi[1]

Mott insulators are paradigmatic examples of strongly correlated physics from which many phases of quantum matter with hard-to-explain properties emerge. Extending the typical SU(2) spin symmetry of Mott insulators to SU(*N*) is predicted to produce exotic quantum magnetism at low temperatures. In this work, we experimentally observe nearest-neighbour spin correlations in a SU(6) Hubbard model realized by ytterbium atoms in optical lattices. We study one-dimensional, two-dimensional square and three-dimensional cubic lattice geometries. The measured SU(6) spin correlations are enhanced compared with the SU(2) correlations, owing to strong Pomeranchuk cooling. The experimental data for a one-dimensional lattice agree qualitatively with our theoretical calculations, with an error of at most 30%, without any fitting parameters. Detailed comparison between theory and experiment allows us to infer the temperature to be the lowest achieved for a cold-atom Fermi–Hubbard model. For three-dimensional lattices, the experiments reach entropies below the regime where our calculations converge, highlighting the importance of these experiments as quantum simulations.

A recurring question regarding many-body quantum systems is how the competition between the kinetic and interaction energies determines the ground-state quantum phases. Quantum fluctuations play an essential role in determining the ground-state spin structure, which may differ drastically from the mean-field prediction. The SU(2) Hubbard model has long been a prototypical system to study these effects, and Hubbard models with an enlarged SU(N) symmetry have attracted great interest.

The study of SU(N) quantum magnetism historically originated from the mathematical technique of large-N expansions[1–4]. More recently, understanding $N>2$ systems has attracted broader interest owing to the expectation that such systems will display a wide array of exotic physics[5–11]. Although N can be large, quantum fluctuations remain important since SU(N) symmetry prevents spins from becoming classical[4,12].

Although theoretical models with SU(N) symmetry have also been discussed in connection with real physical systems such as transition-metal metal oxides[13,14] and graphene's SU(4) spin-valley symmetry[15], the introduction of the symmetry is just a rough approximation. In contrast, an intrinsic SU(N) nuclear spin symmetry[12,16–18] is realized in fermionic isotopes of alkaline earth metal-like atoms (AEAs), providing unique opportunities for quantum simulation experiments of the SU(N) Fermi–Hubbard model (FHM)[19–24]. The SU($N=2I+1$) FHM can be implemented by loading an AEA with a nuclear spin I in an optical lattice. This model is given by the Hamiltonian

$$H=-t\sum_{\langle i,j\rangle,\sigma}c^{\dagger}_{i\sigma}c_{j\sigma}+\frac{U}{2}\sum_{i,\sigma\neq\tau}n_{\sigma}(i)n_{\tau}(i)-\mu\sum_{i,\sigma}n_{\sigma}(i),\qquad(1)$$

where $c_{i\sigma}$ ($c^{\dagger}_{i\sigma}$) denotes the fermionic annihilation (creation) operator for site i, $n_{\sigma}(i)=c^{\dagger}_{i\sigma}c_{i\sigma}$ is the number operator and μ is the chemical potential that controls the density. The flavour index σ labels the projection quantum number of the nuclear spin m_I. Here we employ ^{173}Yb, and m_I is $-5/2, -3/2, \ldots, +5/2$. The tunnelling amplitude t and the on-site interaction U do not depend on σ, giving rise to the SU(N) symmetry.

An important characterization of strongly correlated states is provided by their spin correlation functions. For the SU(2) Hubbard model, antiferromagnetic (AFM) correlations were first observed in dimerized lattices[25], in un-dimerized three-dimensional (3D) lattices using Bragg spectroscopy[26] and in one-dimensional (1D) and two-dimensional (2D) lattices using quantum gas microscopy[27,28]. However, correlations in a uniform SU(N) Hubbard model have not been observed previously. Although observing long-ranged correlations would be essential to characterize phases of matter and their phase transitions, nearest-neighbour spin correlations are already of great interest. In many models, the most rapid change of nearest-neighbour correlations with temperature can be a proxy for the critical temperature, and short-ranged correlations are a key ingredient in pair formation in cuprate and iron-pnictide superconductors, where short-ranged magnetic correlations appear to be essential for the pairing[29,30]. In this work, we observe the nearest-neighbour AFM spin correlations in an SU(6) ^{173}Yb Fermi gas loaded in 1D, 2D and 3D optical lattices and measure them as a function of the initial entropy in a harmonic trap. These experimental results are compared with theoretical calculations with no fitting parameters.

Experimental setup

Figure 1a depicts our physical system. The SU(6) Fermi gas of ^{173}Yb with atom number $N_{\mathrm{ptcl}}=2.4(1)\times10^{4}$ is adiabatically loaded into 1D chain, 2D square and 3D cubic lattices that are constructed by a primary optical lattice operating at 532 nm (Methods). The 1D chain and 2D square lattices are created by introducing strong

---

[1]Department of Physics, Graduate School of Science, Kyoto University, Kyoto, Japan. [2]Department of Physics and Astronomy, Rice University, Houston, TX, USA. [3]Department of Physics, University of Tsukuba, Tsukuba, Japan. [4]Department of Physics, Fudan University, Shanghai, China. [5]Department of Physics, University of California, Davis, CA, USA. ✉e-mail: taie@scphys.kyoto-u.ac.jp

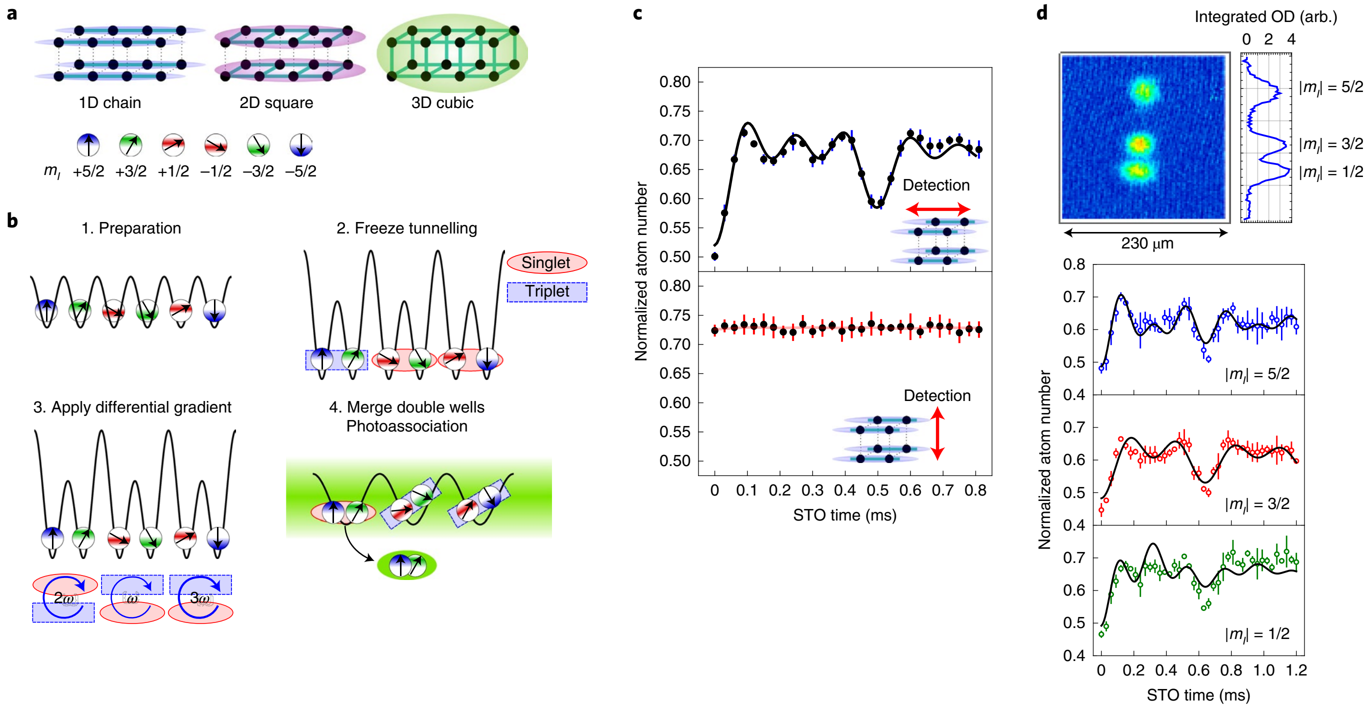

Fig. 1 | Experimental setup. a, SU(6) Hubbard systems realized in various configurations of a 3D optical lattice. Spin components are labelled by the nuclear spin projection quantum number m_I. **b**, Schematic of the experiment. After preparing the equilibrium state (1) and freezing all the tunnelling processes (2), a spin-dependent potential gradient is applied to drive STOs (3). Subsequently, every two adjacent lattice sites are merged into single sites of the detection lattice, followed by PA which removes atom pairs in antisymmetric spin states (4). **c**, Typical example SU(6) STO signals measured for the 1D chain lattice. The spin correlation signal for the nearest neighbours along the chain axis and along the inter-chain direction are shown in the upper and lower graph, respectively. Atom numbers are normalized by the total atom number without molecular association processes, and the deviation from unity represents the fraction of singlet states at each time. The initial entropy per particle is $(1.45\pm0.05)k_B$, and the interaction strength is $U/t=15.3(5)$. The error bars represent the standard deviation for the six independent measurements. **d**, STO measurement with OSG spin separation. Top: Absorption image of the OSG experiment, taken after 5 ms time of flight. Optical density (OD) integrated horizontally is also shown. Bottom: Time evolution of the spin population during STO. The solid lines are fits using the two-frequency model in equation (10). A spin imbalance of 3% is evaluated from the independent measurement with full six-spin separation. The error bars represent the s.e.m. for the three independent measurements.

tunnelling anisotropy into the cubic lattice. The inter-lattice tunnelling is less than 5% of the intra-lattice tunnelling t and is much smaller than the other energy scales in the system. In our previous work[31] we measured the spin correlation of SU(4) fermions loaded into a double-well system in which the nearest-neighbour correlation is artificially enhanced by strong dimerization. However, in the present work, the SU(6) fermions are loaded into uniform lattices in 1D, 2D and 3D in which there is no trivial enhancement of spin correlations due to dimerization.

One can utilize the technique of singlet–triplet oscillations (STO)[25,32] in an optical superlattice to measure the nearest-neighbour correlations, including for SU(N) Fermi gases[31]. The principle of the STO measurement is illustrated in Fig. 1b. Tunnelling is frozen except between pairs of adjacent lattice sites along the measurement axis, which are merged into single sites of a detection lattice with twice the spacing. Here, we utilize the fact that s-wave photoassociation (PA) only associates pairs of atoms with a spatially symmetric wavefunction and thus is only sensitive to spin antisymmetric states in each detection site since the total wavefunction is antisymmetric. Associated molecules quickly escape from the trap, resulting in atom loss. Application of a spin-dependent potential gradient before the merging process drives oscillations of spin symmetry, enabling us to also detect spin symmetric states. In this way, we measure the fraction of both ‘singlet’ and ‘triplet’ states formed within nearest-neighbour lattice sites. The detected SU(N) counterpart of the SU(2) double-well singlet is a $\binom{N}{2}$-fold multiplet with the form $(|\sigma,\tau\rangle-|\tau,\sigma\rangle)/\sqrt{2}$ (where $\sigma\neq\tau$ represents one of the N flavours). Similarly, the double-well triplet is extended to a $\left[\binom{N}{2}+N\right]$-fold multiplet, among which $\binom{N}{2}$ states with the form $(|\sigma,\tau\rangle+|\tau,\sigma\rangle)/\sqrt{2}$ $(\sigma\neq\tau)$ are detected by our scheme while $\sigma=\tau$ is not. In the following, we represent the fraction of atoms forming these ‘singlet’ and detectable ‘triplet’ by P_s and P_{t0}, respectively. These are not to be confused with SU(N) singlets and triplets, which are N-body entangled states[13]. The STO measurement is valid only if the contribution from multiple occupancies can be neglected. For this reason, we set the central density to unit filling and the interaction to be sufficiently strong to suppress double occupancies in the primary lattice. This also maximizes the Pomeranchuk cooling effect because the maximum spin entropy $\ln N$ can be realized only in singly occupied sites. The presence of holes results in double wells containing only a single atom and does not affect STOs.

As a measure for the nearest-neighbour spin correlation, we consider a singlet–triplet imbalance defined as

$$I=\frac{P_s-P_{t0}}{P_s+P_{t0}}. \tag{2}$$

In addition, we consider a normalized STO amplitude

$$A=P_s-P_{t0} \tag{3}$$

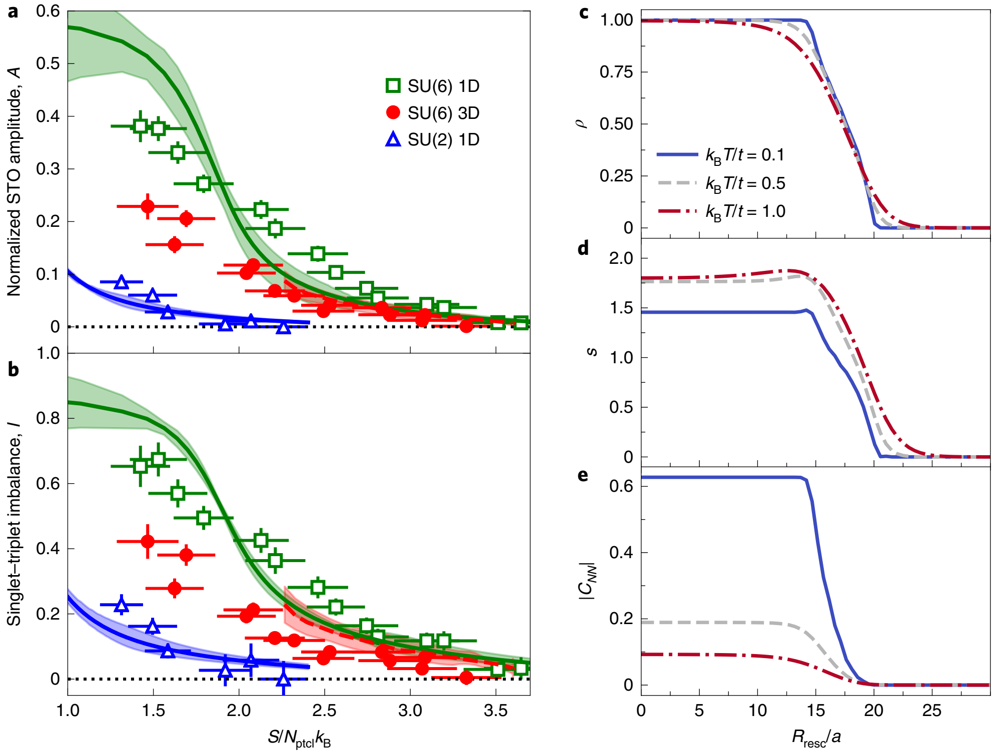

Fig. 2 | Entropy dependence of the nearest-neighbour correlations of the SU(N) FHM at $U/t = 15.3$. a,b, Entropy dependence of the normalized STO amplitude A (**a**) and the singlet–triplet imbalance I (**b**) in 1D and 3D lattices, showing experimental data for the SU(6) 1D (green squares), SU(6) 3D (red circles) and SU(2) 1D systems (blue triangles) with the results of ED (solid lines) and DQMC (dashed lines) calculations. Horizontal error bars represent the s.d. of the ten entropy measurements, while vertical error bars are extracted from the fitting errors in the analysis of the STO signal. Shaded areas represent uncertainty from the systematic and statistical errors of the numerical methods (see Methods for more details), and the possible systematic error (20%) in the total atom number measurement, summed linearly. **c–e**, Observables as a function of distance to the centre of the trap for the 1D system with trap parameters as in the experiments calculated by ED, showing particle number per site (**c**), entropy per site (**d**) and nearest-neighbour spin correlation per site (**e**) as a function of R_{resc}/a, where the rescaled radii are $R_{\mathrm{resc}} = \sqrt{\sum_{a=x,y,z}(\omega_a r_a/\overline{\omega})^2}$, $a = 266$ nm is the lattice constant and $\overline{\omega} = (\omega_x\omega_y\omega_z)^{1/3}$ is the geometric mean of the trapping frequencies, for $N = 6$ at $U/t = 15.3$ in an $L = 8$ site chain at $k_BT/t = 0.1$, 0.5 and 1.0. These temperatures correspond to $S/N_{\mathrm{ptcl}}k_B = 1.75$, 2.17 and 2.54, respectively.

as an alternative measure. As long as the SU(N) symmetry holds, A is proportional to the spatial integration of the SU(N) spin correlation function C_{NN} (ref. [33]) (Methods) given by

$$C_{NN} = \sum_{\sigma\neq\tau}\left[\langle n_\sigma(i)n_\sigma(i+1)\rangle - \langle n_\sigma(i)n_\tau(i+1)\rangle\right], \qquad (4)$$

where $n_\sigma(i+1)$ is a shorthand we use throughout for number operators at a nearest neighbour of i. In the trap, A will be drastically reduced compared with the uniform unit filled case because of the low density at the edge of the sample, and incorporating the effect of the harmonic confinement is important to compare calculations of A with experiments. Note that the singlet and triplet fractions can be determined if we know both I and A.

Figure 1c shows a typical STO signal measured in a 1D chain lattice. To create the spin-dependent potential gradient, we utilize linearly polarized laser light close to the ${}^1S_0 \rightarrow {}^3P_1$ resonant frequency (Methods). As a result, STOs are driven for the spin pairs with different $|m_I|$ values (1/2, 3/2, and 5/2), resulting in three different STO frequencies. The ratio of these frequencies $\omega_{\frac{1}{2}-\frac{3}{2}} : \omega_{\frac{3}{2}-\frac{5}{2}} : \omega_{\frac{5}{2}-\frac{1}{2}} = 1:2:3$ is determined by the Clebsch–Gordan coefficients and does not depend on detuning (Methods). We analyse the STO signal, assuming the SU(N) symmetry, namely that all spin combinations contribute equally to correlations. Along the chain axis, we obtain a singlet–triplet imbalance of $I = 0.674 \pm 0.052$, indicating the large AFM correlation ($C_{NN} < 0$). On the other hand, correlations between chains are zero within the error bar ($I = 0.01 \pm 0.01$) as expected from the negligible inter-chain tunnelling.

To verify the expected SU(6) symmetry, we observe the time evolution of each nuclear spin component during STOs. After the standard STO process (driving STO, merging double wells and applying PA), lattice potentials are ramped down adiabatically in 6 ms to suppress momentum spread. Then, we turn off the optical trap, followed by the application of the optical Stern–Gerlach (OSG) beam for 0.2 ms. The OSG light source is identical to that used for the gradient beam for driving STO but with nearly three times higher intensity. Therefore, the OSG beam is π polarized and distinguishes only spin components with different $|m_I|$. Figure 1d shows analysis of the spin distribution. The behaviour is well reproduced by the two-frequency model (Methods), indicating that the STO scheme is working as designed. The fit to oscillations of the $|m_I| = 1/2$ cloud seems slightly worse than the others. This is due to the stronger deformation of the cloud and possibly spin flips caused by the photon scattering from the OSG laser. We confirm that the deviation of each spin population from the balanced mixture is about 3% and this does not affect the following results.

Results

Antiferromagnetic nearest-neighbour spin correlations. Figure 2a,b shows the nearest-neighbour correlations for the 1D and

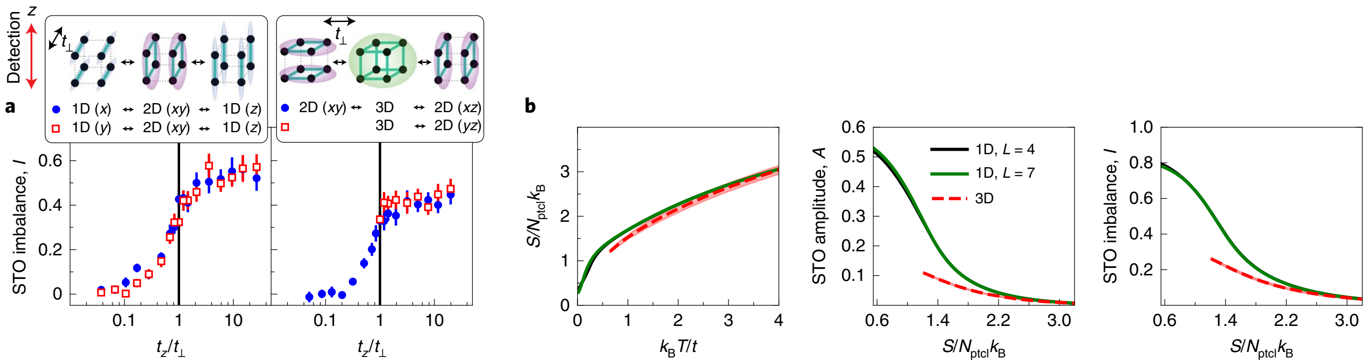

Fig. 3 | Dimension dependence of the spin correlations. **a**, Left: Spin correlations of an SU(6) Fermi gas as the lattice dimensionality is tuned by lattice anisotropy from 1D to 2D. Correlations along the z-axis are measured. Lattices are deformed from x-chains (blue circles) and y-chains (red squares) to z-chains with $U/t=15.3$, via the 2D square lattice with the same U/t. Right: Measurement in 2D–3D crossover. Three possible 2D square lattices are connected via the isotropic 3D cubic lattice at $U/t=15.3$. The initial entropy is $S/N_{\mathrm{ptcl}}k_B=1.4\pm0.1$ for both experiments. The vertical lines indicate the isotropic tunneling $t_z/t_\perp=1$. **b**, The entropy per particle, normalized STO amplitude and singlet–triplet imbalance for $N=3$ in L-site chains and a $4\times4\times4$ cubic lattice for $U/t=8$. Note that the results for $L=4$ and $L=7$ in 1D are nearly identical.

3D lattices as a function of entropy per particle, with a dramatic enhancement of SU(6) spin correlations compared with the SU(2) correlations in the 1D system. The total entropy S is inferred from a time-of-flight measurement of the weakly interacting gas before lattice loading. The on-site interaction is fixed to $U/t=15.3(5)$ for all lattice configurations, which is determined from the band calculation with measured lattice depths. In this strongly interacting regime, an important scale is the maximum spin entropy per particle for a singly occupied site, given by $s^{(N)}_{\mathrm{spin}}=k_B\ln N$, where k_B denotes the Boltzmann constant. Naïvely, ignoring the spatial inhomogeneity of the trap, a sample with $S/N_{\mathrm{ptcl}}<s^{(N)}_{\mathrm{spin}}$ is expected to reach the temperature regime where the spin correlations emerge. For SU(6), $s^{(6)}_{\mathrm{spin}}=1.79k_B$, while for SU(2), $s^{(2)}_{\mathrm{spin}}=0.69k_B$, and $N=6$ systems are therefore expected to show remarkably enhanced correlations, which is interpreted as the enhancement of the Pomeranchuk effect due to large spin[34–36]. Our microscopic theory confirms this simple picture, and the observed data show reasonable agreement with theoretical predictions obtained by exact diagonalization (ED) for 1D and by determinantal quantum Monte Carlo (DQMC) for 3D, without any fitting parameters.

Here, we suggest a possible origin of the small deviation observed between the theory and experiment. Given the extensive tests we have done on our codes and experiments, we consider an actual error in the calculations or the experiments unlikely. The remaining possibility is the fundamental differences between the model being simulated and the atomic system being measured. On the computational side, we have carefully investigated Trotter errors, finite-size effects and the use of the local density approximation (LDA) (Methods). The calculations assume that the loading is adiabatic, while non-adiabatic loading of the atoms to the lattice may play some role in the experiments. For the 1D SU(6) case, the correlations measured in the low-entropy region are smaller than the theoretical curve by ~30%, and it is plausible that the main source of the discrepancy is the non-adiabaticity of the lattice loading. We estimate the amount of heating to be $0.2k_B$ around the lowest temperature (Methods). For the higher-entropy region in the 1D SU (6) case, on the other hand, the measured correlations are larger than the theoretical predictions. Although experiments start with a weakly interacting gas, it is possible that some of the initial correlations are frozen during lattice loading, which could be a source of the small remaining discrepancies between the experimental results and theory.

Figure 2c–e shows theoretically calculated trap profiles of atom number, entropy and nearest-neighbour spin correlations per site for a 1D system. A rigid Mott plateau is well developed at $k_BT/t\approx0.5$, and spin correlation develops rapidly for lower temperature. Estimation of the temperature obtained in our experiment is discussed in the next section.

Extracting temperature in an optical lattice by theory–experiment comparison. The present experiments cannot directly measure the temperature at the very low entropies studied here. However, for the 1D systems, the temperature can be inferred by comparing experiment and theory. In 1D, the lowest temperature achieved in the experiments is $k_BT/t=0.096\pm0.054\pm0.030$, obtained from the singlet–triplet imbalance I measured experimentally at $S/N_{\mathrm{ptcl}}k_B=1.45\pm0.05$ (Extended Data Fig. 1). The first error is an estimate of the finite-size error given by the difference between the finite-size extrapolation to the thermodynamic limit and the eight-site result. The second error comes from the experimental uncertainty on the correlations. This is lower than the state-of-the-art temperatures reported in cold-atom FHM systems[26,28,37–39]. Estimates based on A rather than I are similar (Methods). The agreement between theory and experiment in 1D suggests the reliability of the experiment in higher dimensions where numerics fail and quantum simulation via experiment is crucial.

For comparison, at the same entropy, the SU(2) system is at $k_BT/t=1.008\pm0.073\pm0.001$, or to obtain the same singlet–triplet imbalance, the SU(2) system should be at $S/N_{\mathrm{ptcl}}k_B=0.499\pm0.136\pm0.120$. Since the state-of-the-art averaged entropy per particle for SU(2) experiments with alkali atoms is around $1k_B$ (ref. [28]), this suggests an experimental advantage for SU(N) systems in obtaining highly correlated states in optical lattices.

Dependence on lattice dimensionality. In addition to the dependence on N, the correlations depend drastically on dimensionality, with the 1D case exhibiting the largest correlations as shown in Fig. 3a,b. This behaviour is similar to previous studies in an SU(2) system[40–42] and can be understood at sufficiently high temperatures. In this regime, correlations depend only on temperature not dimension (this intuitive result can be proved with a high-temperature expansion) and decrease with increasing temperature. Additionally, decreasing dimension decreases the bandwidth and thus, at fixed entropy, decreases the temperature (Fig. 3b). Together, these imply that correlations decrease as the dimensionality is increased. The situation at lower temperatures is expected to be more complicated, but the numerics indicate that this simple conclusion remains true.

Constructing simple arguments for the low-temperature regime remains an interesting challenge.

Figure 3a shows the singlet–triplet imbalance measured through 1D–2D and 2D–3D crossovers with the same initial condition. We measure the correlations along the z-axis and change the ratio of t_z to the tunnelling $t_\perp$ of the initially weak link. At both the maximum and minimum $t_z/t_\perp$ and at the intermediate point $t_z/t_\perp = 1$, we set $U/t_z = 15.3$. The lattice geometry is changed smoothly between the above three points (see also Methods). We find that spin correlations decrease monotonically as the lattice is deformed from 1D to 2D. For the 2D–3D crossover, the difference is smaller but the trends of decreasing correlations with increasing dimensionality are still visible. The correlation drops quickly for $t_z/t_\perp < 1$ and becomes undetectable, as expected.

Numerical calculations show a similar trend. Although DQMC has difficulty in obtaining reliable results for 3D systems at the low temperatures where remarkable correlations develop for $U/t = 15.3$ and $N = 6$, it can calculate the properties of 3D systems for $U/t = 8$ and $N = 3$ to low temperature where remarkable correlations develop. Because we are considering a smaller N, we calculate ED results without using the basis state truncation for 1D L-site chains with $L = 4$–7. Figure 3b presents the computed entropy per particle and the spin correlations. Although these are not directly the conditions in the experiments, they do show the same trend of correlations decreasing with increasing dimension.

DQMC results for $N = 6$ are only presented at temperatures above $T/t = 1$, owing to a strong sign problem below this temperature, as well as the onset of non-ergodicities in the Monte Carlo sampling in this region. The sign problem is particularly strong in the metallic region, where large errors in the observables appear for several values of the chemical potential. Reference [43] provides more details on how the sign problem depends on U/t and μ/t.

Discussion

We find that the measured nearest-neighbour AFM correlations agree broadly with the theory with no fitting parameters for all temperatures in 1D, and at temperatures where converged theoretical results can be obtained in 3D. In our work for 3D lattices, we have entered the region where converged theoretical calculations are unavailable and quantum simulation manifests its usefulness.

While we successfully demonstrate the lowest temperature achieved in the FHM in our 1D optical lattice experiment, there is still room for reaching even lower temperatures, for example, by engineering spatial redistribution of entropy[28].

The STO measurement presented here is also applicable to spin-imbalanced cases by introducing proper oscillation functions. On the other hand, the spin structures measured in this work are limited to the SU(2)-type nearest-neighbour singlets and triplets. In general SU(N) systems, more nontrivial spin states arise. For example, the SU(N) singlet given by the fully antisymmetric combination of N spins plays an essential role in SU(N) antiferromagnets. Probing such multi-spin entanglement will be an important experimental challenge. Measuring the long-range correlations is also of interest. One of the most important questions that has not yet been answered is whether the long-range ordering persists in the SU(N) system. Measuring long-range correlations will be feasible by using a quantum gas microscope with a spin-selective detection technique. State-of-the-art numerical and analytic calculations, with the use of approximations, have proposed a variety of possible ground states such as flavour-ordered patterns and valence bond solids, among others[5–11]. Experiments are now poised to discriminate finite-temperature analogues of such proposed states.

Online content

Any methods, additional references, Nature Research reporting summaries, source data, extended data, supplementary information, acknowledgements, peer review information; details of author contributions and competing interests; and statements of data and code availability are available at https://doi.org/10.1038/s41567-022-01725-6.

Received: 12 March 2021; Accepted: 15 July 2022;
Published online: 1 September 2022

References

1. Read, N. & Newns, D. M. On the solution of the Coqblin–Schreiffer Hamiltonian by the large-N expansion technique. *J. Phys. C* **16**, 3273–3295 (1983).
2. Affleck, I. Large-N limit of SU(N) quantum "spin" chains. *Phys. Rev. Lett.* **54**, 966–969 (1985).
3. Bickers, N. E. Review of techniques in the large-N expansion for dilute magnetic alloys. *Rev. Mod. Phys.* **59**, 845–939 (1987).
4. Auerbach, A. *Interacting Electrons and Quantum Magnetism* (Springer-Verlag, 1994).
5. Tóth, T. A., Läuchli, A. M., Mila, F. & Penc, K. Three-sublattice ordering of the SU(3) Heisenberg model of three-flavor fermions on the square and cubic lattices. *Phys. Rev. Lett.* **105**, 265301 (2010).
6. Bauer, B. et al. Three-sublattice order in the SU(3) Heisenberg model on the square and triangular lattice. *Phys. Rev. B* **85**, 125116 (2012).
7. Nataf, P. & Mila, F. Exact diagonalization of Heisenberg SU(N) models. *Phys. Rev. Lett.* **113**, 127204 (2014).
8. Corboz, P., Läuchli, A. M., Penc, K., Troyer, M. & Mila, F. Simultaneous dimerization and SU(4) symmetry breaking of 4-color fermions on the square lattice. *Phys. Rev. Lett.* **107**, 215301 (2011).
9. Hermele, M. & Gurarie, V. Topological liquids and valence cluster states in two-dimensional SU(N) magnets. *Phys. Rev. B* **84**, 174441 (2011).
10. Romen, C. & Läuchli, A. M. Structure of spin correlations in high-temperature SU(N) quantum magnets. *Phys. Rev. Res.* **2**, 043009 (2020).
11. Yamamoto, D., Suzuki, C., Marmorini, G., Okazaki, S. & Furukawa, N. Quantum and thermal phase transitions of the triangular SU(3) Heisenberg model under magnetic fields. *Phys. Rev. Lett.* **125**, 057204 (2020).
12. Wu, C. Hidden symmetry and quantum phases in spin-3/2 cold atomic systems. *Mod. Phys. Lett. B* **20**, 1707–1738 (2006).
13. Li, Y. Q., Ma, M., Shi, D. N. & Zhang, F. C. SU(4) theory for spin systems with orbital degeneracy. *Phys. Rev. Lett.* **81**, 3527–3530 (1998).
14. Tokura, Y. Orbital physics in transition-metal oxides. *Science* **288**, 462–468 (2000).
15. Goerbig, M. O. Electronic properties of graphene in a strong magnetic field. *Rev. Mod. Phys.* **83**, 1193–1243 (2011).
16. Cazalilla, M. A., Ho, A. F. & Ueda, M. Ultracold gases of ytterbium: ferromagnetism and Mott states in an SU(6) Fermi system. *N. J. Phys.* **11**, 103033 (2009).
17. Gorshkov, A. V. et al. Two-orbital SU(N) magnetism with ultracold alkaline-earth atoms. *Nat. Phys.* **6**, 289–295 (2010).
18. Cazalilla, M. A. & Rey, A. M. Ultracold Fermi gases with emergent SU(N) symmetry. *Rep. Prog. Phys.* **77**, 124401 (2014).
19. Affleck, I. & Marston, J. B. Large-n limit of the Heisenberg–Hubbard model: implications for high-T_c superconductors. *Phys. Rev. B* **37**, 3774–3777 (1988).
20. Honerkamp, C. & Hofstetter, W. Ultracold fermions and the SU(N) Hubbard model. *Phys. Rev. Lett.* **92**, 170403 (2004).
21. Assaad, F. F. Phase diagram of the half-filled two-dimensional SU(N) Hubbard–Heisenberg model: a quantum Monte Carlo study. *Phys. Rev. B* **71**, 075103 (2005).
22. Hermele, M., Gurarie, V. & Rey, A. M. Mott insulators of ultracold fermionic alkaline earth atoms: underconstrained magnetism and chiral spin liquid. *Phys. Rev. Lett.* **103**, 135301 (2009).
23. Del Re, L. & Capone, M. Selective insulators and anomalous responses in three-component fermionic gases with broken SU(3) symmetry. *Phys. Rev. A* **98**, 063628 (2018).
24. D., Tusi et al. Flavour-selective localization in interacting lattice fermions via SU(N) symmetry breaking. Preprint at https://arxiv.org/abs/2104.13338 (2021).
25. Greif, D., Uehlinger, T., Jotzu, G., Tarruell, L. & Esslinger, T. Short-range quantum magnetism of ultracold fermions in an optical lattice. *Science* **340**, 1307–1310 (2013).
26. Hart, R. A. et al. Observation of antiferromagnetic correlations in the Hubbard model with ultracold atoms. *Nature* **519**, 211–214 (2015).
27. Boll, M. et al. Spin- and density-resolved microscopy of antiferromagnetic correlations in Fermi–Hubbard chains. *Science* **353**, 1257–1260 (2016).
28. Mazurenko, A. et al. A cold-atom Fermi–Hubbard antiferromagnet. *Nature* **545**, 462–466 (2017).
29. Scalapino, D. J. Superconductivity and spin fluctuations. *J. Low Temp. Phys.* **117**, 179–188 (1999).
30. Paglione, J. & Greene, R. L. High-temperature superconductivity in iron-based materials. *Nat. Phys.* **6**, 645–658 (2010).

31. Ozawa, H., Taie, S., Takasu, Y. & Takahashi, Y. Antiferromagnetic spin correlation of SU(*N*) Fermi gas in an optical superlattice. *Phys. Rev. Lett.* **121**, 225303 (2018).
32. Trotzky, S., Chen, Y.-A., Schnorrberger, U., Cheinet, P. & Bloch, I. Controlling and detecting spin correlations of ultracold atoms in optical lattices. *Phys. Rev. Lett.* **105**, 265303 (2010).
33. Manmana, S. R., Hazzard, K. R. A., Chen, G., Feiguin, A. E. & Rey, A. M. SU(*N*) magnetism in chains of ultracold alkaline-earth-metal atoms: Mott transitions and quantum correlations. *Phys. Rev. A* **84**, 043601 (2011).
34. Taie, S., Yamazaki, R., Sugawa, S. & Takahashi, Y. An SU(6) Mott insulator of an atomic Fermi gas realized by large-spin Pomeranchuk cooling. *Nat. Phys.* **8**, 825–830 (2012).
35. Bonnes, L., Hazzard, K. R. A., Manmana, S. R., Rey, A. M. & Wessel, S. Adiabatic loading of one-dimensional SU(*N*) alkaline-earth-atom fermions in optical lattices. *Phys. Rev. Lett.* **109**, 205306 (2012).
36. Messio, L. & Mila, F. Entropy dependence of correlations in one-dimensional SU(*N*) antiferromagnets. *Phys. Rev. Lett.* **109**, 205306 (2012).
37. Parsons, M. F. et al. Site-resolved measurement of the spin-correlation function in the Fermi–Hubbard model. *Science* **353**, 1253–1256 (2016).
38. Cheuk, L. W. et al. Observation of spatial charge and spin correlations in the 2D Fermi–Hubbard model. *Science* **353**, 1260–1264 (2016).
39. Hofrichter, C. et al. Direct probing of the Mott crossover in the SU(*N*) Fermi–Hubbard model. *Phys. Rev. X* **6**, 021030 (2016).
40. Imriška, J. et al. Thermodynamics and magnetic properties of the anisotropic 3D Hubbard model. *Phys. Rev. Lett.* **112**, 115301 (2014).
41. Greif, D., Jotzu, G., Messer, M., Desbuquois, R. & Esslinger, T. Formation and dynamics of antiferromagnetic correlations in tunable optical lattices. *Phys. Rev. Lett.* **115**, 260401 (2015).
42. Ibarra-García-Padilla, E. et al. Thermodynamics and magnetism in the two-dimensional to three-dimensional crossover of the Hubbard model. *Phys. Rev. A* **102**, 033340 (2020).
43. Ibarra-García-Padilla, E. et al. Universal thermodynamics of an SU(*N*) Fermi–Hubbard model. *Phys. Rev. A* **104**, 043316 (2021).

Methods

Sample preparation. A degenerate Fermi gas of ^{173}Yb is prepared by evaporative cooling in a crossed dipole trap operating at 532 nm. The optical lattice also has the wavelength 532 nm and the simple cubic geometry. The additional detection lattices at 1,064 nm along the z- and x-axes are used only for STO measurement. In the main result obtained in Fig. 2, the optical lattices are ramped up to $\mathbf{s} = (s_x, s_y, s_z) = (7.0, 7.0, 7.0)$ for the 3D cubic lattice, $(6.1, 20.0, 6.1)$ for the 2D (x–z) square lattice and $(20.0, 20.0, 5.0)$ for the 1D (z-)chain lattice. Here, $s_{x,y,z}$ are the lattice depths in units of the recoil energy $E_{\rm R} = \hbar^2(2\pi/\lambda)^2/2m$ with atomic mass m and the wavelength of the lattice laser beams $\lambda = 532$ nm, where $\hbar$ is the reduced Planck constant. In the dimensional crossover experiment shown in Fig. 3, the lattice geometry is changed smoothly in the form $\mathbf{s} = (1-p)\mathbf{s}_1 + p\mathbf{s}_2$ $(0 < p < 1)$, where $\mathbf{s}_1$ and $\mathbf{s}_2$ take the values given above for definite dimensionalities, as well as $(6.1, 6.1, 20)$ for 2D (x–y) square and $(5.0, 20.0, 20.0)$ for 1D (x-)chain lattices. The dipole trap together with the optical lattice creates an overall harmonic potential for the sample, whose trap frequencies are $(\omega_{x'}, \omega_{y'}, \omega_z) = 2\pi \times (102, 44, 155)$ Hz for the 3D lattice, $2\pi \times (105, 49, 158)$ Hz for the 2D lattice and $2\pi \times (107, 54, 162)$ Hz for the 1D lattice. The principal axes of the trap x' and y' are tilted by 45° from the lattice axes x and y, within the horizontal plane. For the experiment shown in Extended Data Fig. 2, the trap frequency depends weakly on U/t with the variations within 10%.

The entropies of atomic gases are calculated numerically using the temperature obtained by fitting the Thomas–Fermi distribution to time-of-flight images of harmonically trapped samples. The effect of the repulsive interaction is evaluated within mean-field theory, which predicts entropies up to 6% higher than that of non-interacting gases. The effect of interaction during cloud expansion causes an additional systematic error in the entropy, which is estimated to be smaller than 10%. Trap anharmonicity is also evaluated, and we conclude that the correction is no more than 5% of the pure harmonic value.

Non-adiabatic heating is observed during the lattice loading process. We compare the spin correlations after the normal loading and the 'round-trip' process in which we once decrease the lattice down to the minimum depth where evaporation is negligible, followed by ramping up again. This results in the decrease of the singlet–triplet imbalance by 50–60% for all lattice configurations, corresponding to one-way heating of $0.2k_{\rm B}$ per atom in the 1D case. This is consistent with the widely used method of measuring the entropy increase after the gas loaded to and released from the lattice potential, which in our case implies a heating of $(0.15–0.35)k_{\rm B}$.

SU(6) STO. To generate a spin-dependent potential gradient, we apply an optical Stern–Gerlach laser beam close to the $^1S_0 \rightarrow {}^3P_1$ resonance. The detuning of +2.6 GHz from the $F = 5/2 \rightarrow 7/2$ transition is selected to minimize the ratio of the photon scattering rate to the differential light shifts.

The STO signal is analysed by comparing the total atom number with the number of atoms remaining after removing singlets by PA via the resonance that is located at −812 MHz from the $^1S_0 \rightarrow {}^3P_1$ $(F = 7/2)$ transition[31]. Assuming that the SU(6) symmetry is not broken, the functional form of the time evolution of the remaining atom number is

$$N(t) = -a\exp(-t/\tau)\left[\cos\omega t + \cos 2\omega t + \cos 3\omega t\right] + b, \qquad (5)$$

with fitting parameters a, b, τ and ω. The oscillation frequency ω is determined from the differential light shift of each spin pair. In general, a differential light shift of a pair (m_I, m_I') is of the form $\sum_{F'} f(\delta_{F'})[C(F', m_I) - C(F', m_I')]$, where f is a function of the detuning $\delta_{F'}$ from the excited hyperfine states F' and $C(F', m_I)$ is the transition strength. The constant frequency ratio $(\omega, 2\omega, 3\omega)$ follows from the fact that, for linear polarization, $[C(F', m_I) - C(F', m_I')]$ can be reduced to the separated form $C'(F')R(m_I, m_I')$. Photon scattering and the inhomogeneity of the gradient due to the Gaussian shape of the OSG beam with intensity ~15 W cm^{-3} cause a decay of the STO signal, which is described by the exponential decay term in equation (5). The gradient beam propagates along the y-axis, and the measurement along the z-axis is chosen to suppress the effect of inhomogeneity.

Among the $\binom{6}{2} = 15$ spin combinations relevant to STO, linearly polarized light gives rise to the differential light shifts for 12 combinations with different absolute values of m_I. The remaining three combinations with the same $|m_I|$ do not show STO. Therefore, the singlets formed by these pairs are always removed by PA during STOs, and the corresponding triplets always remain in the trap. Taking this fact into account, the singlet and triplet fractions in the SU(6) case are expressed as

$$P_{\rm s} = \frac{1}{N_{\rm ptcl}}\left[N_{\rm ptcl} - D + 3a - b\right], \qquad (6)$$

$$P_{\rm t0} = \frac{1}{N_{\rm ptcl}}\left[N_{\rm ptcl} - D - \frac{9a}{2} - b\right]. \qquad (7)$$

where $N_{\rm ptcl}$ is the total atom number without PA and D is the number of atoms on doubly occupied sites (typically less than 3% of $N_{\rm ptcl}$), which are measured independently without merging and STO processes. Multiple occupancies higher than double are negligibly small. PA light causes also one-body loss induced by photon scattering, which gives rise to an overestimate of the two-body PA loss. In the presence of one-body loss, the substitution $N(t) \rightarrow e^{\gamma\tau_{\rm PA}}N(t)$ is required in analysing STO, where γ is the one-body loss rate and $\tau_{\rm PA}$ is the PA pulse duration. In our experiment, γ is found to be 0.3% of the PA rate and the correction to $N(t)$ is typically 1%. In the SU(2) case, the STO is a simple sinusoid and the analogous expressions are

$$P_{\rm s} = \frac{1}{N_{\rm ptcl}}\left[N_{\rm ptcl} - D + a - b\right], \qquad (8)$$

$$P_{\rm t0} = \frac{1}{N_{\rm ptcl}}\left[N_{\rm ptcl} - D - a - b\right]. \qquad (9)$$

An atom with specific $|m_I|$ can show STOs with two possible frequencies. With OSG separation, the time evolution of the atom number in each separated cloud $N_{|m_I|}$ is described by the two-frequency oscillation

$$N_{|m_I|}(t) = -a\exp(-t/\tau)\left[\cos\omega_{|m_I|,1}t + \cos\omega_{|m_I|,2}t\right] + b, \qquad (10)$$

with oscillation frequencies

$$(\omega_{|m_I|,1}, \omega_{|m_I|,2}) = \begin{cases} (\omega, 3\omega) & |m_I| = 1/2 \\ (\omega, 2\omega) & |m_I| = 3/2 \\ (2\omega, 3\omega) & |m_I| = 5/2. \end{cases} \qquad (11)$$

Figure 1d agrees well with these behaviours of equation (10), confirming the validity of the present analysis of STO.

Numerical calculations for homogeneous systems. DQMC and ED calculations are used to obtain the values of the thermodynamic quantities, including the density, entropy and nearest-neighbour spin correlation function for homogeneous systems. These results are used to compute the properties for the trapped system using the LDA, which is described below.

ED results were obtained in L-site chains by performing full diagonalization over a reduced Hilbert space (described below) and using finite-size scaling. For computational efficiency, we exploit two aspects of the SU(N) symmetry. Particle number conservation for each spin flavour

$$[N_\sigma, H] = 0 \qquad (12)$$

with $N_\sigma = \sum_j n_\sigma(j)$ and the translation symmetries allow us to block-diagonalize the Hamiltonian. Furthermore, we exploit the spin permutation symmetries

$$\left[S^\sigma_\tau, H\right] = 0, \qquad \forall\sigma, \tau = 1, \ldots, N \qquad (13a)$$

with

$$S^\sigma_\tau = \sum_i S^\sigma_\tau(i) = \sum_i c^\dagger_{i\sigma}c_{i\tau}, \qquad (13b)$$

which relate many of the sectors of the Hamiltonian, and therefore one needs to diagonalize only one representative from each sector.

In addition to the (exact) symmetries, we employ a basis state truncation, which we converge systematically. First, the Hilbert space only includes states with total particle number less than or equal to a fixed particle number $N_{\rm max}$. Second, it omits states if the total on-site energy (the energy associated with the presence of multiple occupancies in the cluster) is larger than $E_{\rm cut}$. We present results obtained from $N_{\rm max} = L + 1$ and $E_{\rm cut} = U$ for $L = 5–7$ and $N_{\rm max} = L$ for $L = 8$. Extended Data Fig. 3 shows that the results for the STO amplitude versus entropy with these truncations are converged to ~10^{-5}.

DQMC results for 4×4 square and 4×4×4 cubic lattices were obtained by introducing $N(N-1)/2$ auxiliary Hubbard–Stratonovich fields, one for each interaction term $n_{i\sigma}n_{i\tau}$. Note that previous works applied DQMC to the half-filled SU(2N) FHM using a different, discrete complex Hubbard–Stratonovich decomposition[44,45]. Following our new approach, DQMC calculations for fillings below 1.5 particles per site at $U/t = 15.3$ can be obtained reliably for temperatures $k_{\rm B}T \geq t$. At lower temperatures, correlation functions become inaccessible to DQMC owing to sign and ergodicity problems. DQMC data were obtained for five different random seeds, each with 8,000 sweeps through the lattice and the $N(N-1)/2$ auxiliary fields for equilibration and 10,000 sweeps for measurements. The inverse temperature was discretized as $\beta = L\Delta\tau$ with a Trotter step of $\Delta\tau = 0.025/t$. Results are obtained in μ–T grids with $d\mu = 0.25$ and dT given by the Trotter step for all integers $L \geq 2$. These results are linearly interpolated before computing the entropy and using the LDA. The entropy per site is computed as the integral of the specific heat, which by thermodynamic relations can be rearranged to

$$s(\mu, T) = N\log(2) + \frac{f(\mu, T)}{T} - \int_T^\infty \frac{f(\mu, T')}{T'^2}\,dT', \qquad (14)$$

where $f=\epsilon-\mu n$, and ϵ and n are the energy and particle number per site, respectively. To accelerate convergence, we obtain DQMC results up to a temperature cut-off T_{cut} and use the leading-order high-temperature series term ($t=0$) in the integral in equation (14) for $T>T_{\mathrm{cut}}$.

LDA. Local values of thermodynamic quantities and correlation functions are obtained using the LDA, which replaces intensive observables at a spatial location $\mathbf{r}$ with their value in a homogeneous system with chemical potential $\mu(\mathbf{r})=\mu_0-V(\mathbf{r})$, where μ_0 is the global chemical potential and $V(\mathbf{r})$ is the external confinement. Applied to the total particle number and the total entropy, this gives

$$N_{\mathrm{ptcl}}=\int\frac{\mathrm{d}^3r}{a^3}\,n(\mu_0-V(\mathbf{r}),T), \tag{15}$$

$$S=\int\frac{\mathrm{d}^3r}{a^3}\,s(\mu_0-V(\mathbf{r}),T), \tag{16}$$

where n/a^3 and s/a^3 are the density and entropy density calculated for the homogeneous system. The variables that can be measured experimentally are N_{ptcl} and S rather than μ_0 and T, but given the homogeneous functions $n(\mu,T)$ and $s(\mu,T)$, then μ_0 and T can be obtained from N_{ptcl} and S by solving equations (15) and (16) numerically.

As derived below, the STO amplitude A and imbalance I are related to the correlation C_{NN}, defined in equation (4), and to the correlation $\langle n(i)n(i+1)\rangle$ by

$$A=-\frac{1}{N_{\mathrm{ptcl}}}[C_{NN}]_{\mathrm{tot}}, \tag{17}$$

$$I=\frac{2A}{\frac{1}{N_{\mathrm{ptcl}}}[n(i)n(i+1)]_{\mathrm{tot}}+A} \tag{18}$$

in the LDA, where we define

$$[\mathcal{O}]_{\mathrm{tot}}=\int\frac{\mathrm{d}^3r}{a^3}\langle\mathcal{O}(\mu(\mathbf{r}),T)\rangle. \tag{19}$$

In practice, we calculate plots of observable versus T or S as follows: First, we calculate a list of points (T,μ_0) where μ_0 is obtained by solving equation (15) for given T and the particle number N_{ptcl} measured in experiment. Then, for each such obtained (T,μ_0), we calculate S and other trap-summed observables of interest. In this way, we plot trap-summed observables as functions of T. Details on the grid used and discretization error introduced are given below.

Trap geometry. Owing to the large atomic mass of Yb, the effect of gravity is severe for our optical trap, especially in the final stage of evaporative cooling (Extended Data Fig. 4a). To include the anharmonic effect in our LDA calculation, we evaluate the density of state (DOS) defined as

$$D(E)=\frac{\partial\Sigma}{\partial E},\quad \Sigma(E)=\sum_{\text{lattice sites }i}\Theta\left(E-\tilde{V}(\mathbf{r}_i)\right), \tag{20}$$

where $\tilde{V}(\mathbf{r}_i)$ is the full external potential at the site i except the periodic part forming optical lattices. Note that this DOS function becomes exact only in the atomic limit $t\to 0$ but is always valid for use in the LDA integral described below. Trap-summed observables are calculated using equations (15)–(19). These integrals over space are then rewritten as integrals over energy with the DOS:

$$[\mathcal{O}]_{\mathrm{tot}}=\int\mathrm{d}E\,D(E)\langle\mathcal{O}(\mu_0-E,T)\rangle. \tag{21}$$

In the harmonic approximation, the DOS is given by

$$D(E)=\frac{2\pi}{a^3}\left(\frac{2}{m\bar{\omega}^2}\right)^{3/2}E^{1/2}, \tag{22}$$

where $\bar{\omega}$ is the geometric mean of the trap frequencies.

Extended Data Fig. 4b shows the evaluated DOS for the 3D cubic lattice. In calculating equation (20), we exclude the spatial region outside the potential barrier, where $\tilde{V}(\mathbf{r}_i)$ becomes a uniformly decreasing function along the direction of gravity (Extended Data Fig. 4a). In the low-energy region, the DOS is well reproduced by the harmonic approximation. As energy increases, the DOS starts to exceed the harmonic prediction due to the nearly flat potential where the optical potential gradient is competing with the gravitational one. For even higher energies, the DOS falls below the harmonic approximation because the contribution is limited to only from the upper half of the trap. The difference between the results calculated in the harmonic approximation and using the full potential is small, never larger than 2.4×10^{-2} for the normalized STO amplitude and imbalance in the range of entropies presented herein.

STO amplitude and imbalance. In the limit where there are no multiple occupancies, the populations in the singlet and triplet states $p^{\mathrm{s}}_{\sigma\tau}(i)$ and $p^{\mathrm{t0}}_{\sigma\tau}(i)$ for an STO with spin components σ and τ in the dimer located on sites i and $i+1$ are given by the expectation value of the projection operators

$$\begin{aligned}\widehat{P}^{\mathrm{s}}_{\sigma\tau}(i)=\tfrac{1}{2}\;&\left(c^{\dagger}_{i,\sigma}c^{\dagger}_{i+1,\tau}-c^{\dagger}_{i,\tau}c^{\dagger}_{i+1,\sigma}\right)\\&\times\left(c_{i+1,\tau}c_{i,\sigma}-c_{i+1,\sigma}c_{i,\tau}\right),\end{aligned} \tag{23}$$

$$\begin{aligned}\widehat{P}^{\mathrm{t0}}_{\sigma\tau}(i)=\tfrac{1}{2}\;&\left(c^{\dagger}_{i,\sigma}c^{\dagger}_{i+1,\tau}+c^{\dagger}_{i,\tau}c^{\dagger}_{i+1,\sigma}\right)\\&\times\left(c_{i+1,\tau}c_{i,\sigma}+c_{i+1,\sigma}c_{i,\tau}\right).\end{aligned} \tag{24}$$

Note that these refer to SU(2) singlets involving components σ and τ rather than SU(N) singlets. It is useful to introduce spin-1/2 operators $S^z_{\sigma\tau}(i)=[n_\sigma(i)-n_\tau(i)]/2$ for the pair of states σ and τ. By the SU(N) symmetry, the population difference and sum are equal to[25]

$$p^{\mathrm{s}}_{\sigma\tau}(i)-p^{\mathrm{t0}}_{\sigma\tau}(i)=-4\langle S^z_{\sigma\tau}(i)S^z_{\sigma\tau}(i+1)\rangle, \tag{25}$$

$$\begin{aligned}p^{\mathrm{s}}_{\sigma\tau}(i)+p^{\mathrm{t0}}_{\sigma\tau}(i)=&+\tfrac{1}{2}\langle n(i)n(i+1)\rangle\\&-2\langle S^z_{\sigma\tau}(i)S^z_{\sigma\tau}(i+1)\rangle.\end{aligned} \tag{26}$$

The fractions of atoms forming singlets $P_{\mathrm{s}}=N_{\mathrm{s}}/N_{\mathrm{ptcl}}$ and triplets $P_{\mathrm{t0}}=N_{\mathrm{t0}}/N_{\mathrm{ptcl}}$ are obtained from a sum over each dimer in the lattice, or equivalently $(1/2)\sum_i\cdots$, and all the possible σ–τ spin pairs,

$$P_{\mathrm{s}}=\frac{2}{N_{\mathrm{ptcl}}}\left[\frac{1}{2}\sum_i\left(\frac{1}{2}\sum_{\sigma\neq\tau}p^{\mathrm{s}}_{\sigma\tau}(i)\right)\right], \tag{27a}$$

$$P_{\mathrm{t0}}=\frac{2}{N_{\mathrm{ptcl}}}\left[\frac{1}{2}\sum_i\left(\frac{1}{2}\sum_{\sigma\neq\tau}p^{\mathrm{t0}}_{\sigma\tau}(i)\right)\right]. \tag{27b}$$

Therefore, the global STO amplitude is

$$A=P_{\mathrm{s}}-P_{\mathrm{t0}}=\sum_i\sum_{\sigma\neq\tau}\left[\frac{-4\langle S^z_{\sigma\tau}(i)S^z_{\sigma\tau}(i+1)\rangle}{2N_{\mathrm{ptcl}}}\right], \tag{28}$$

which in terms of the $n_\sigma(i)$ is

$$\begin{aligned}A&=-\sum_i\sum_{\sigma\neq\tau}\left[\frac{\langle n_\sigma(i)n_\sigma(i+1)\rangle-\langle n_\sigma(i)n_\tau(i+1)\rangle}{N_{\mathrm{ptcl}}}\right]\\&=-\frac{1}{N_{\mathrm{ptcl}}}\sum_i C_{NN}(i).\end{aligned} \tag{29}$$

The STO imbalance I is defined as

$$I=\frac{P_{\mathrm{s}}-P_{\mathrm{t0}}}{P_{\mathrm{s}}+P_{\mathrm{t0}}}, \tag{30}$$

so

$$I=\frac{2A}{\frac{1}{N_{\mathrm{ptcl}}}\sum_i\langle n(i)n(i+1)\rangle+A}, \tag{31}$$

where $\langle n(i)n(i+1)\rangle$ is the density–density correlation function. Equations (29)–(31) directly yield equations (17) and (18).

Thermometry in 1D. Extended Data Fig. 1 shows how we determine the lowest temperature achieved in the 1D experiments ($k_{\mathrm{B}}T/t=0.096\pm0.054\pm0.030$). Estimates based on A rather than I give a similar result. The estimate based on the lowest entropy before lattice loading predicts a somewhat lower temperature, although still consistent within error bars. A small increase in temperature could result from non-adiabatic effects during the lattice loading. Extended Data Fig. 2 shows the interaction dependence of the spin correlations. The tendency towards larger discrepancy between theory and measurement with larger interactions (equivalent to deeper lattice depths) suggests that heating is important for deeper lattices.

ED error estimates. Errors for the ED results arise from two sources: finite-size error and truncation of the Hilbert space using the on-site energy and maximum particle number criteria. Extended Data Fig. 5 presents the normalized STO amplitude and imbalance for SU(2) and SU(6) in 1D for different system sizes of $L=5$–8, as well as the finite-size extrapolation. Results in the main text are presented after finite-size scaling at fixed entropy per particle, which is performed by fitting the results for $L = 5$–8 to $\mathcal{O}_L = \mathcal{O}_\infty + m/L$ with $\mathcal{O}_\infty$ and m as fitting parameters. Validity of the Hilbert space truncation is tested by varying the energy cut-off E_{cut} as well as the maximum particle number $N_{\max}$. Extended Data Fig. 3 demonstrates that, for the interaction strengths considered herein, the truncation is extremely accurate, with no visible differences for any parameters.

DQMC error estimates. The DQMC results have several sources of error, which are estimated and presented in Extended Data Table 1 for SU(6) and $U/t = 15.3$ and in Extended Data Table 2 for SU(3) at $U/t = 8$. All error estimates are presented after the adiabatic loading calculation obtained by calculations for a $4\times4\times4$ lattice at $k_BT/t = 1$ unless explicitly stated otherwise. In this section, we briefly discuss how each error source was estimated.

The largest and most difficult to quantify error comes from finite-size effects. As a proxy, we estimate finite-size effects in two different ways. Our first estimate is a spot check comparison between the $3\times3\times3$ and $4\times4\times4$ systems at fixed T/t and density. We obtain $C_{NN}(4\times4\times4) = -0.096 \pm 0.004$ and $C_{NN}(3\times3\times3) = -0.125 \pm 0.005$ at the lowest temperature ($T/t = 1$) for a homogeneous system at $\langle n\rangle = 1$, and this error decreases rapidly with increasing temperature. Note that this error may be dominated by the error of the smaller, $3\times3\times3$ system rather than reflecting the smaller error in the $4\times4\times4$ system. Our second estimate is by studying 2D, and taking the difference between the 4×4 results and the 6×6 results for the full computations of LDA-averaged observables. Larger system sizes, in particular in 3D, remain inaccessible at present.

The inverse temperature discretization error is estimated as the difference of the results obtained with Trotter steps of $\Delta\tau = 0.025$ and $\Delta\tau = 0.05$.

The entropy per site s at temperature T is given by equation (14). Errors in the calculation of s arise from the finite value of the temperature cut-off T_{cut}. This error was estimated in the homogeneous case by comparing the results obtained with $k_BT_{\mathrm{cut}}/t = 500$, 800 and 1,000.

Errors in numerical integration procedures such as the LDA summing of observables in the trap and the computation of the entropy are estimated by varying the coarseness of the μ–T integration grids. Such estimations were obtained by coarsening them by a factor of two and comparing the results.

Statistical errors are presented for both the homogeneous case and after adiabatic loading for five different random seeds. These errors are presented as the s.e.m.

Data availability

All the data presented in this paper are available from the corresponding author upon reasonable request.

Code availability

The mathematical codes that support the findings of the study are available from the corresponding author upon reasonable request.

References

44. Wang, D. et al. Competing orders in the 2D half-filled SU(2*N*) Hubbard model through the pinning-field quantum Monte Carlo simulations. *Phys. Rev. Lett.* **112**, 156403 (2014).
45. Zhou, Z., Cai, Z., Wu, C. & Wang, Y. Quantum Monte Carlo simulations of thermodynamic properties of SU(2*N*) ultracold fermions in optical lattices. *Phys. Rev. B* **90**, 235139 (2014).

Acknowledgements

We thank H. Ozawa for contributions in the early stage of the experiment. The experimental work was supported by JSPS grants-in-aid for scientific research nos. JP17H06138, JP18H05405 and JP18H05228, the Impulsing Paradigm Change through Disruptive Technologies (ImPACT) programme, JST CREST (no. JPMJCR1673) and MEXT Quantum Leap Flagship Program (MEXT Q-LEAP) grant no. JPMXS0118069021. Y. K. acknowledges the support of the Grant-in-Aid for JSPS Fellows (no. 17J00486). The work of K.R.A.H., E.I.-G.-P. and H.-T.W. was supported in part by the Welch Foundation through grant no. C1872 and the National Science Foundation through grant no. PHY1848304. The work of R.T.S. was supported by grant DE-SC0014671 funded by the U.S. Department of Energy Office of Science.

Author contributions

S.T., N.N. and Y. Takasu carried out experiments. S.T. analysed the data. Y.K. gave advice on experiments from the theoretical viewpoint. Y. Takahashi conducted the whole experiment. E.I.-G.-P. developed the SU(*N*) DQMC code extended from R.T.S.'s SU(2) code, performed the DQMC calculations, many ED calculations and the LDA calculations with ED and DQMC results, and carried out the theoretical data analysis. H.-T.W. developed the ED code and performed many of the ED calculations. R.T.S. and K.R.A.H. conceived and supervised the theoretical calculations. E.I.-G.-P., H.-T.W., R.T.S. and K.R.A.H. all contributed to interpreting the theory and theory–experiment comparisons. All the authors contributed to preparing the manuscript. S.T. and E.I.-G.-P. contributed equally to this work.

Competing interests

The authors declare no competing interests.

Additional information

The online version contains supplementary material available at https://doi.org/10.1038/s41567-022-01725-6.

Correspondence and requests for materials should be addressed to Shintaro Taie.

Peer review information *Nature Physics* thanks Peter Schauß and the other, anonymous, reviewer(s) for their contribution to the peer review of this work.

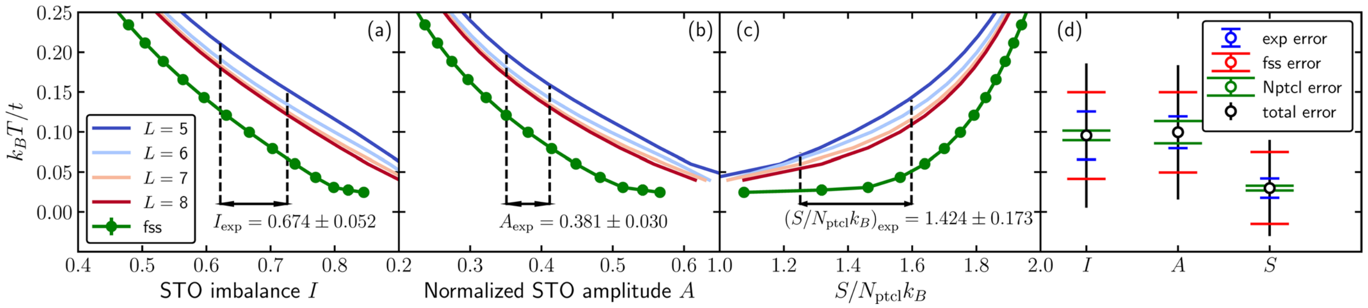

Extended Data Fig. 1 | Temperature of a 1D SU(6) Fermi gas at *U/t* = 15.3. The vertical dashed lines indicate the range of the largest experimentally measured STO imbalance in 1D that is consistent with error bars. The temperature of this datapoint is inferred from the finite-size scaling curves and the results are summarized in panel (d). The fss error is a conservative estimate of the finite-size error, the difference between the finite-size scaled results and the *L* = 8 site chain. The exp error comes from the experimental uncertainty on the correlations.

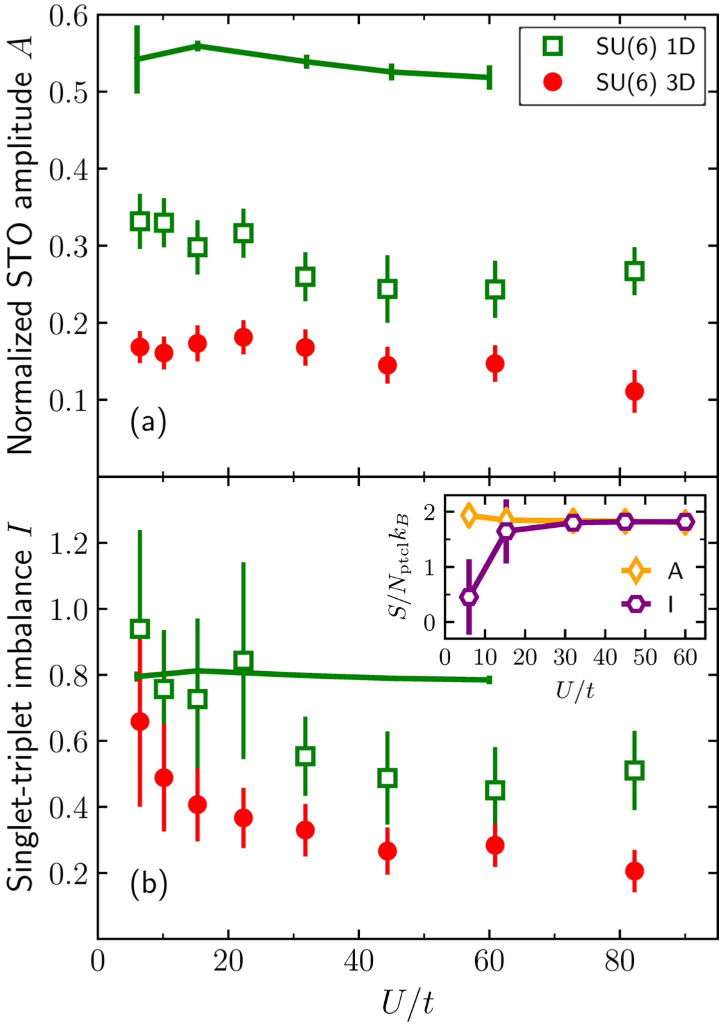

Extended Data Fig. 2 | Interaction dependence of the nearest neighbor correlations. Behavior of (a) STO amplitude and (b) singlet-triplet imbalance in 1D and 3D lattices are shown. Experimental data is shown for SU(6) systems with initial entropy $S/N_{\rm ptcl}k_B = 1.4 \pm 0.1$. The error bars are extracted from the error of fit in the analysis of the STO signal. Solid lines are the result of exact diagonalization calculations for $S/N_{\rm ptcl}k_B = 1.4$, and the error bars correspond to the sum in quadrature of the finite-size error and the basis-state truncation error. The inset presents the entropy per particle extracted by fitting it to reproduce the experimentally measured spin correlations. Results saturate at $S/N_{\rm ptcl}k_B = 1.818 \pm 0.005$. Error bars in the inset come from the experimental uncertainty on the correlations.

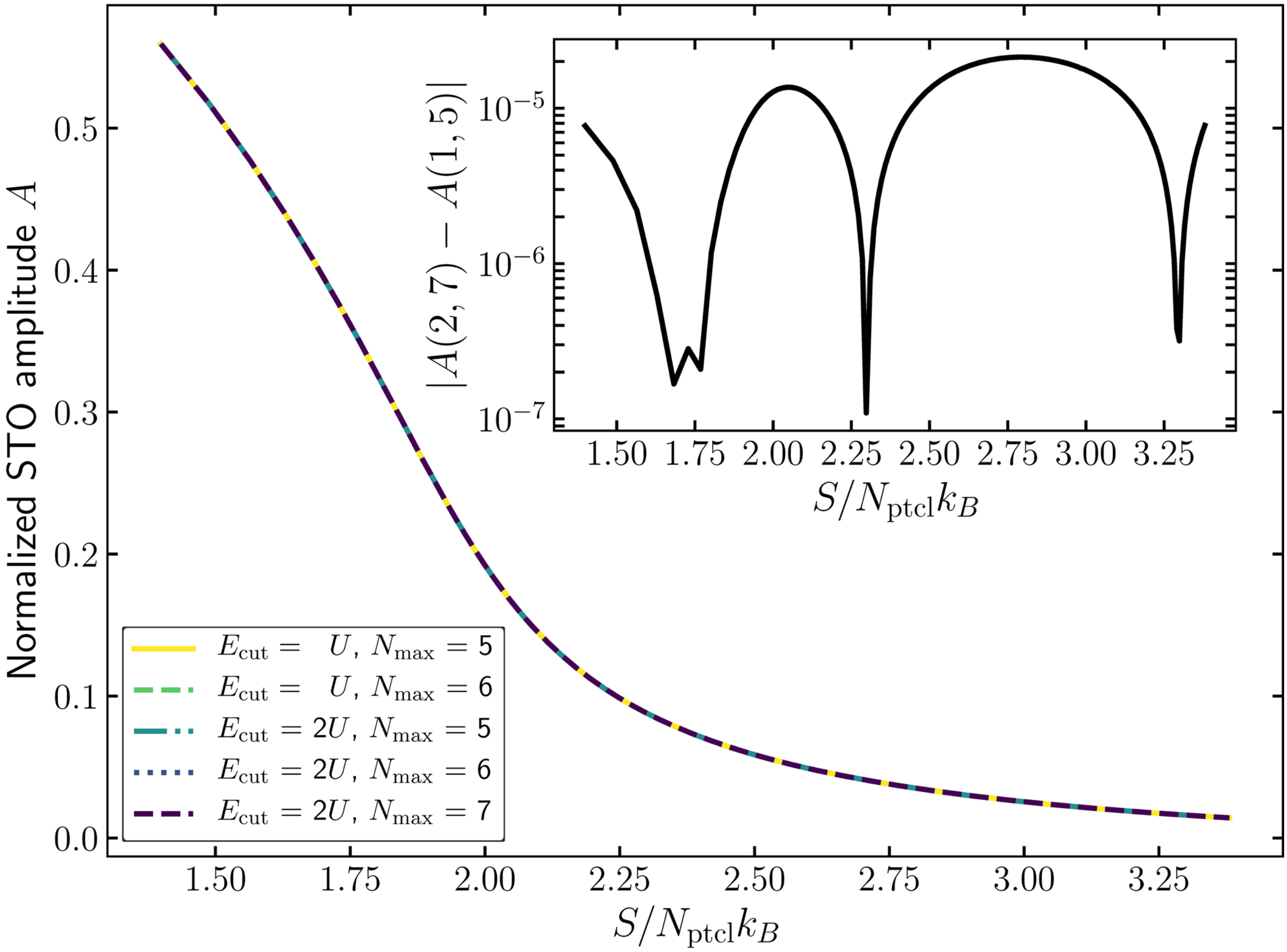

Extended Data Fig. 3 | Normalized STO amplitude for an SU(6) Fermi gas in an $L = 5$ site chain with $U/t = 15.3$ for different truncations of the Hilbert space. Basis states with an on-site energy larger than the energy cutoff E_{cut}, as well as those that exceed the maximum particle number N_{max} are disregarded. There is no visible difference between calculations. The inset shows the absolute value of the difference between the $E_{\mathrm{cut}} = 2U$, $N_{\mathrm{max}} = 7$ and $E_{\mathrm{cut}} = U$, $N_{\mathrm{max}} = 5$ curves.

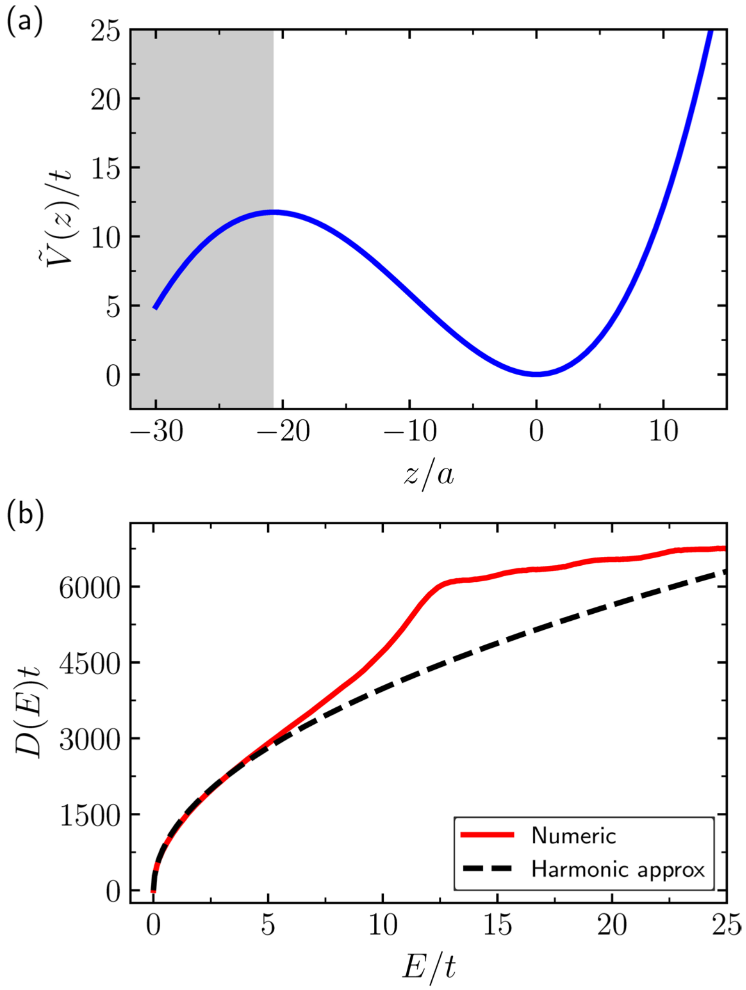

Extended Data Fig. 4 | Trap anharmonicity. (a) Full external potential (optical + gravity) profile along the direction of gravity *z*. The shaded region is excluded from the calculation of DOS. (b) Density of states calculated from the external potential for the 3D cubic geometry. The corresponding harmonic approximation is also shown. The atoms are sensitive only to the density of states for $E/t \lesssim 10$.

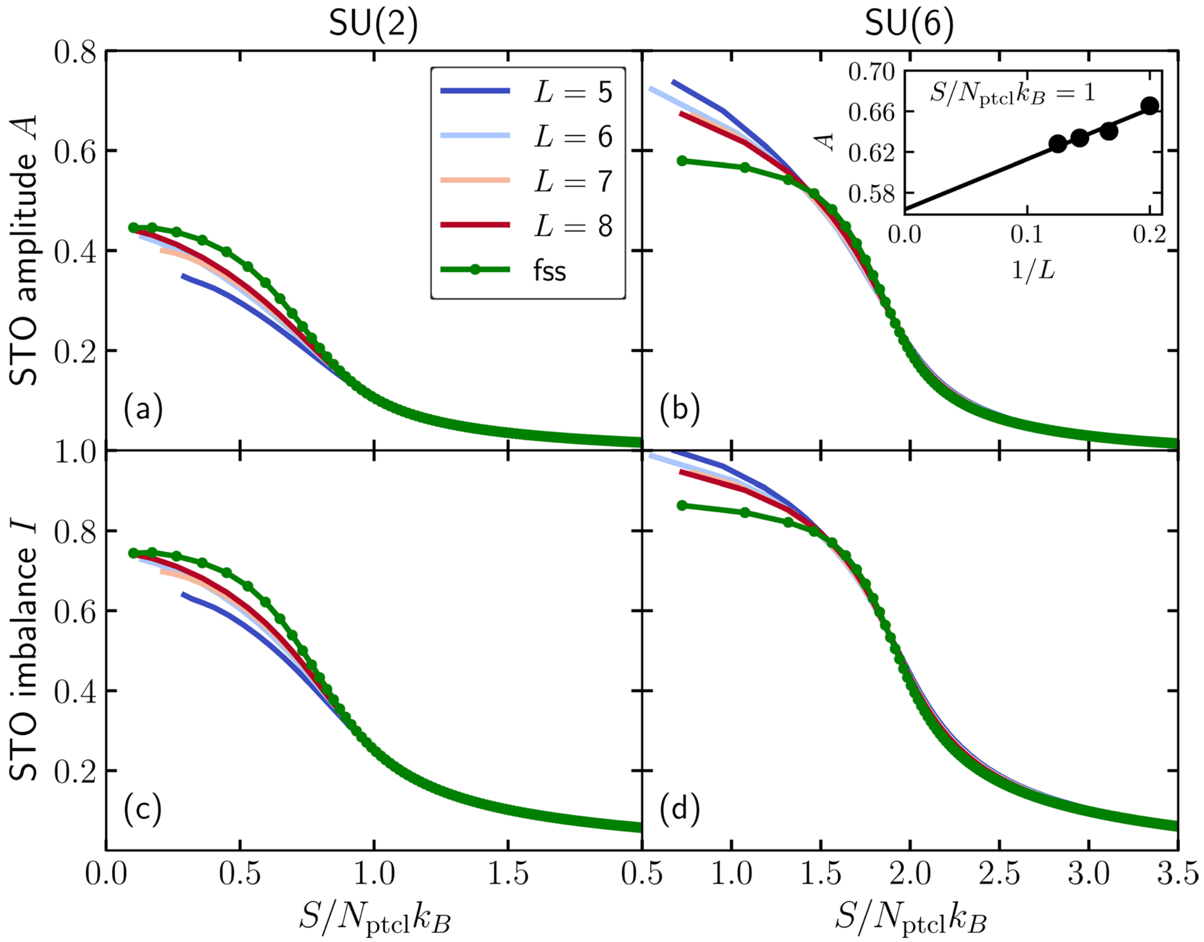

Extended Data Fig. 5 | Finite-size scaling in 1D. Normalized STO amplitude and imbalance for SU(2) and SU(6) Fermi gases in *L*-site chains and the results after finite-size scaling (fss) for $U/t = 15.3$. The inset in panel (b) illustrates the finite-size scaling procedure.

Error source (homogeneous, worst case over all μ and T)	S vs T	A vs T	I vs T
Finite T_{cut}	1.3×10^{-4}	–	–
Statistical	1.2×10^{0}	1.8×10^{-1}	8.6×10^{-2}
Error source (in the trap)	S vs T	A vs S	I vs S
Finite size (2D)	1.8×10^{-2}	1.1×10^{-2}	2.4×10^{-2}
Trotter-step	1.8×10^{-2}	4.6×10^{-3}	9.5×10^{-3}
μ grid coarseness	6.9×10^{-3}	7.2×10^{-3}	1.5×10^{-2}
T grid coarseness	1.4×10^{-2}	2.4×10^{-3}	5.3×10^{-3}
Statistical (adiabatic loading)	1.0×10^{-2}	1.6×10^{-3}	3.2×10^{-3}

Extended Data Table 1 | Error estimates for the DQMC calculation at $U/t = 15.3$. Errors are presented at $k_B T/t = 1$. Most errors decrease with increasing temperature. The top two rows estimate errors by considering homogeneous systems as follows: "Finite T_{cut}" is the error by a non-infinite value of T_{cut} in entropy integrations estimated by the difference of $k_B T_{cut} = 1000$ and 500. "Statistical" estimates is the standard error of the mean, taken at its largest value over all μ and T considered. The bottom 5 rows come from results after adiabatic loading in the trap, as follows. "Finite size (2D)" is the finite-size error estimated by the difference between $A(S)$ in 4×4 and 6×6 geometries, "Trotter-step" is the Trotter error estimated by the difference of $A(S)$ for Trotter step size $\Delta\mu = 0.05$ and 0.025, "μ-grid coarseness" and "T-grid coarseness" are the estimates of the errors associated with discretizing μ and T by taking the difference of the result after doubling the grid spacing, and "Statistical (adiabatic loading)" is the standard error of the mean of the DQMC.

Error source	S vs T	A vs S	I vs S
Trotter-step	3.2×10^{-2}	7.8×10^{-4}	2.1×10^{-3}
μ grid coarseness	7.8×10^{-4}	1.6×10^{-4}	5.2×10^{-4}
T grid coarseness	1.3×10^{-1}	1.8×10^{-3}	4.9×10^{-3}
Statistical (adiabatic loading)	2.0×10^{-4}	5.0×10^{-5}	1.2×10^{-4}

Extended Data Table 2 | Error estimates for the different error sources involved in the DQMC calculation for $U/t=8$ and $N=3$. Row labels are the same as in Extended Data Table 1. The first three rows are for homogeneous systems while the last is for the A(S) after adiabatic loading. For homogeneous system results, we report the largest error in the whole range of temperatures/entropies considered. The T grid coarseness error for S vs T monotonically increases from 2.0×10^{-2} at $k_BT/t=0.64$ to the value reported in the table, 1.3×10^{-1}, at $k_BT/t=4$.